Photothermally tunable Fabry-Pérot fiber interferometer for photoacoustic mesoscopy

Bohua Chen,[1] Yuwen Chen,[1] and Cheng Ma[1,2,3,*]

[1]*The Department of Electronic Engineering, Tsinghua University, Beijing, 100084, China*
[2]*Beijing National Research Center for Information Science and Technology, Beijing 100084, China*
[3]*Beijing Innovation Center for Future Chip, Beijing 100084, China*
[*]*cheng_ma@mail.tsinghua.edu.cn*

Abstract: An optical fiber based Fabry-Pérot interferometer whose resonant wavelength can be dynamically tuned was designed and realized for photoacoustic mesoscopy. The optical path length (OPL) of the Fabry-Pérot cavity can be modulated by a photothermal heating process, which was achieved by adjusting the power of a 650 nm heating laser. The optical heating process can effectively change the thickness and refractive index of the polymer spacer of the sensor cavity. The robustness of the sensor can be greatly improved by proper packaging. The interferometer was interrogated by a relatively cheap wavelength-fixed 1550 nm laser for broadband and sensitive ultrasound detection, eliminating the requirement for an expensive tunable interrogation laser. The sensing module was then integrated into a photoacoustic mesoscopic imaging system. Two phantom imaging experiments and an *ex vivo* imaging experiment demonstrated the capability of such a miniature sensor. The interferometer has an acoustic detection bandwidth of up to 30 MHz and a noise equivalent pressure of 40 mPa/Hz$^{1/2}$ (i.e., 220 Pa over the full detection bandwidth). The new tuning mechanism and the batch-production compatibility of the sensor holds promises for commercialization and parallelized detection.

1. Introduction

Photoacoustic tomography (PAT), an imaging modality with high-resolution, optical contrast and deep penetration [1], has potential applications in clinical practices such as breast [2–4], dermatologic [5–9], and vascular imaging [10–12]. In PAT systems, short laser pulses illuminate biological tissue to excite photoacoustic (PA) signals. Chromophores like hemoglobin, lipid or melanin in tissue absorb photons and generate instant heat due to nonradiative transition. The instant heating of tissue generates ultrasound pulses via thermoelastic expansion. After distributed detection of the ultrasound pulses, one can reconstruct a tomogram of spectrally resolved light absorption. Unlike in traditional biomedical ultrasound, the generated PA pulses cover several kHz to hundreds of MHz, extend a broad emission angle, and are relatively weak, with peak pressure on the order of kPa and below. In the reconstructed tomogram, image resolution and fidelity hinge on the richness of the temporal and spatial frequencies in the detected PA signals. Limited temporal and spatial (angular) bandwidths limit image resolution and can cause problems such as 'limited view' [13,14].

The above requirements pose great challenge for ultrasound detection in PA imaging. According to image resolution and penetration depth, PA imaging can be classified into PA microscopy, PA mesoscopy and PA macroscopy. PA microscopy aims at cellular, or even subcellular resolutions, while its penetration is typically confined to within 1 mm. PA macroscopy has imaging depths of more than 10 mm, while the detection bandwidth is typically less than 10 MHz (corresponding to an acoustically defined resolution of 100~500 μm). PA mesoscopy bridges the gap between these two scales and provides resolutions down to ten microns and penetration depths of a few millimeters [15,16]. In this relatively new imaging scale, PA mesoscopy encounters challenges associated with signal detection, namely, its spatial resolution greatly exceeds PA macroscopy (i.e.,

larger bandwidth), and its penetration extends much beyond optical-resolution PA microscopy (i.e., higher sensitivity). Due to their potential broadband and sensitive acoustic detection ability, optical ultrasound sensors including interferometric [17–23] and non-interferometric sensors [24–26] have been designed and applied in PA imaging and other ultrasound applications. Among these various sensors, Fabry-Pérot interferometer (FPI) has been extensively studied and demonstrated useful [12,19,27–34], especially high-finesse FPI. The planar FPI fabricated by Zhang *et al*. had a noise equivalent pressure (NEP) of 210 Pa over 20MHz bandwidth, or 47.0mPa/Hz$^{1/2}$[19]. The finesse of planar FPI is relatively low due to the "walk-off" effect inside the FP cavity and limits the acoustic detection performance [35]. An improved scheme to enhance the finesse is to fabricate FPI with plano-concave cavity. This FPI has stronger light confinement compared to the planar one. The best NEP obtained by plano-concave FPIs by Guggenheim *et al*. was 1.6mPa/Hz$^{1/2}$ [35]. Besides, this plano-concave FPI can be fabricated on the endface of an optical fiber, which brings extra advantages such as small footprint and easier optical alignment. The fiber based FPI shows excellent sensitivity with NEP of 2.1mPa/Hz$^{1/2}$ over 20MHz bandwidth and its response can reach up to 40MHz. Even though great progress has been made with these FPIs, there are still some problems when it comes to sensor interrogation. For the planar FPI, thickness uniformity is an issue, which makes interrogation complex, expensive, and slow. Fabricating planar FPIs with optically-uniform thickness can be costly and challenging. One method for interrogation is to tune the interrogation laser wavelength to the optimal value and acquire acoustic signal point by point [19]. This method is time-consuming and costly. Another method employs the electro-optical effect or electro-mechanical effect to actively control the cavity thickness by applying a voltage in a distributed manner [36]. For the fiber based FPI, each sensing element requires a high-power, wavelength-tunable, narrow-linewidth and mode-hopping-free continuous wave (CW) laser for interrogation. This kind of laser is much more expensive than ordinary single mode laser diodes (LD), making paralleled detection costly. As shown in [35,37–41], fiber-based FPIs enjoy advantages including high sensitivity, broadband and wide-angle detection, and small footprint, thus, we envision wide range applications of such sensors in PA imaging and beyond if the system interrogation cost can be greatly reduced.

In this work, we propose and realize a photothermally tuned FPI, capable of real-time spectral tuning for sensitive, wide-angle, broadband ultrasound detection. By moderately doping the sensor cavity with a metal complex solvent dye which exhibits specific absorption at 650 nm, we obtain a resonant wavelength-tunable interferometer with tuning range up to 5nm. The resonant wavelength can be tuned by altering the incident power of a 650 nm heating laser in a feedback loop. After carefully packaging the tunable interferometer in a photoacoustic mesoscopic system, we accomplished a detection NEP of 40 mPa/Hz$^{1/2}$ over a detection bandwidth of 30 MHz. This design allows for a relatively cheap laser diode with a narrow linewidth and fixed output wavelength as the interrogation laser. Subsequently, a significant reduction of system cost is achieved. Using this sensor, we obtained good-quality PA mesoscopic images of two different phantoms and an *ex vivo* mouse kidney.

2. Sensor fabrication and characterization

As shown in Fig. 1(a), a plano-concave microcavity is built on the cleaved end-face of a section of stripped double clad fiber (DCF, Nufern SM-9/105/125-20A). To enhance the quality factor of the resonator, the cleaved DCF end-face should have a cleaving angle as small as possible (which means the fiber axis should be perpendicular to the cutting plane; an ideal cleaving angle should be 0° with respect to the perpendicular plane. Limited by the performance of the fiber cleaver, it is hard to obtain an ideal cleaving angle in our experiments), and a highly clean surface. Figure 1(b) shows a microscopic view of a home-made fiber-based interferometer, obtained by a CCD camera (MR-H200SCP) with a magnification of 360. The DCF can deliver light of two different colors simultaneously. The fiber core with a diameter of 9 μm is used to transmit 1550

nm narrow-linewidth interrogation laser, while the inner clad with a diameter of 105μm guides a multimode beam of 650 nm, heating the cavity to suitable optical path length (OPL). The Fabry-Pérot cavity is formed by a pair of highly reflective mirrors. The mirror can be dielectric mirror or metal mirror (for the outer one), here we use distributed Bragg reflector (DBR) based dielectric mirrors. The first mirror attaches to the DCF tip while the second mirror is a spherical cap covering the whole cavity. Both mirrors are fabricated by vacuum evaporating 9 alternating layers of silicon dioxide (SiO_2) and titanium dioxide (TiO_2), to a designed reflectivity of >98% at 1550nm. The sensor cavity is made by dip-coating to form an ultraviolet-cured polymer (UV glue, Norland 61) spacer. The dip-coating and curing processes are as follows: (1) Prepare a mixture of the UV glue and the metal complex solvent dyes (Nanjing Haozhuo, dark blue color). The mass ratio between the UV glue and the dyes is 40:1. (2) After thoroughly stirred, vacuum the mixture using a vacuum pump (Fujiwara 750D) to remove bubbles for 30 minutes. (3) The fibers (with dielectric mirrors already coated on one side) are fixed in a customized holder so that 29 fibers can be dip-coated simultaneously. The holder is mounted on a motorized translation stage (Daheng Optics, GCD-101050M) and the fibers are perpendicular to the mixture surface. (4) Lower the stage so that the fiber end-faces are immersed into the mixture to a depth around 1 mm. Then with a moving velocity of 1 mm/s, the stage moves upwards to pull out the fibers from the mixture. (5) A 16 W UV lamp (composed of two lamp tubes: PHILIPS TL 8W/05) is used to cure the polymer coating for 2 hours. After curing, the samples are ready for the second dielectric mirror deposition to form the FPIs. Figure 1(c) shows the transmittance of the colored polymer spacer material (we used a thickness~200 μm for the transmission test). This material shows strong optical absorption centered around 600 nm, while exhibits superb transparency at the C band. This spectral property allows us to effectively heat the cavity by the 650 nm laser, while the 1550 nm interrogation light is almost unaffected. The OPL of the micro-cavity is determined by the refractive index and physical thickness of the polymer spacer, both can be tuned by temperature. The coefficient of thermal expansion (CTE) of the cured UV glue is about 2.5×10^{-4}/°C while the rate of change of refractive index versus temperature is about -1.6×10^{-4}/°C. The equivalent coefficient of thermal expansion of OPL C_{eq} can be formulated as below:

$$C_{eq} \;=\; CTE + \frac{\Delta n}{n\Delta T} \tag{1}$$

where $n \approx 1.5$ is the refractive index of polymer spacer and $\Delta n/\Delta T$ is the rate of change of refractive index versus temperature. The estimated C_{eq} is about 1.4×10^{-4}/°C. Being illuminated by the 650 nm laser, the polymer spacer expands, the amount of which is controlled by the laser power. Figure 1(d) plots the resonant wavelength of a FPI against the incident optical power of the 650 nm laser. It shows clearly that the resonant wavelength can be tuned almost linearly by changing the power of the heating laser. This capability provides the basis for dynamic tuning of the interferometer during operation, moreover, it relaxes the tolerance of the sensor thickness during fabrication. The resonant wavelength λ depends on the physical thickness d of the cavity as $\lambda = 2nd/m$, where n is optical refractive index of polymer spacer, and m is a positive integer defined by the order of the resonant dip. In our case, $\lambda = 1550$ nm, d ≈ 20 μm, n ≈ 1.5. If the resonant dip at m = 40 is selected, then the accurate spacer thickness should be 20.667 μm. In practice, it is almost impossible to achieve a thickness accuracy down to the nanometer level during fabrication. This problem is greatly alleviated by photo-thermal tuning, while the thickness tolerance Δd is redefined by the tuning range $\Delta\lambda$: $\Delta d = m\Delta\lambda/(2n)$. For a wavelength tuning range of 10nm, the thickness tolerance of the Fabry-Pérot cavity is relaxed to 0.133 μm. The fact that many diode lasers in the C band are tunable within a small wavelength range further relaxes the sensor thickness tolerance, making batch production of the sensor feasible. More specifically, in our experiment, twenty nine fibers can be processed simultaneously for dip-coating and curing, with relatively high uniformity. During the dielectric mirror deposition

process, hundreds of samples can be fabricated with very high uniformity. As a result, the cost for fabricating a single FPI sensor decreases dramatically.
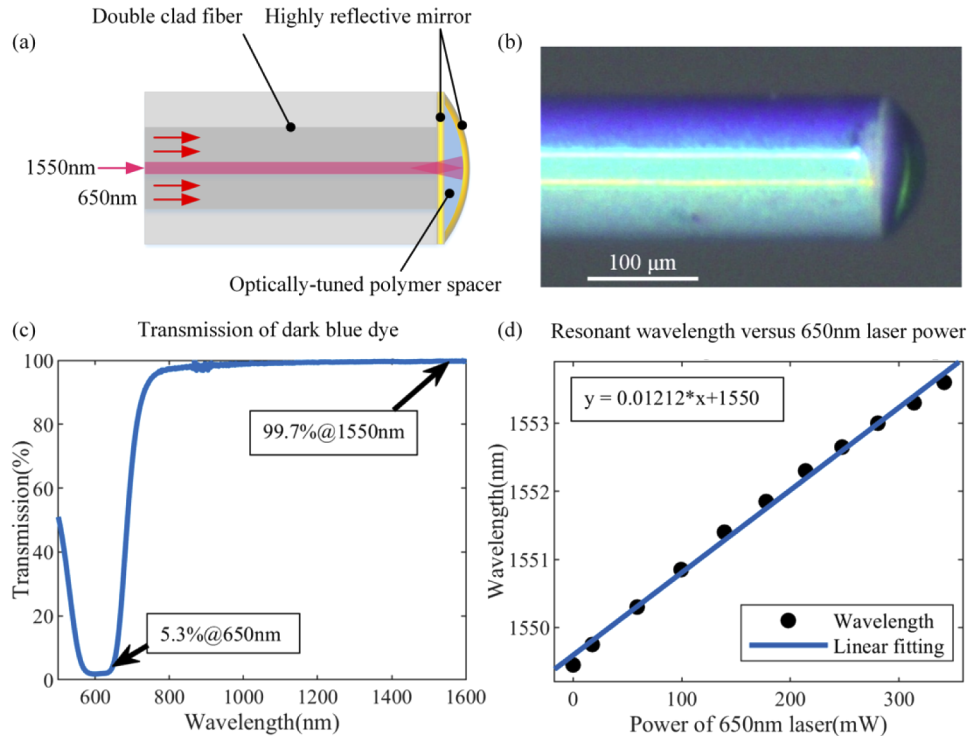

Fig. 1. (a) Schematic of the interferometer. (b) Microscopic view of the sensor head. (c) Transmission spectrum of a 200 µm thick spacer sample doped with dark blue metal complex solvent dye. (d) Experimentally measured resonant wavelength versus power of the heating laser shows linear operation.

The interferometric sensors were characterized optically and acoustically. Figure 2(a) provides the reflection spectrum of a representative FPI measured with a C-band amplified spontaneous emission (ASE, MAX-RAY PHOTONICS ASE-C-20-M) source and an optical spectrum analyzer (OSA, Agilent 86140B). Limited to the resolution of the OSA (the smallest resolution is 60 pm), reflectance near resonant wavelength of the interferometer can't be resolved accurately. Due to instrumental restrictions, the measured full-width half-maximum (FWHM) of the resonant dip was larger than the real value (the difference was approximately the resolution, 60 pm), the fringe visibility was smaller than the real value, while the free spectral range was relatively accurate. Other parameters related to the FPI can be calculated with the measured results. Typical values for these parameters are listed in Table 1. We also performed a theoretical analysis based on finite element analysis using the COMSOL software, and the result is co-plotted in Fig. 2(a). Geometrical and optical parameters in the simulation were tuned to match that of the FPI used in the experiment. In particular, a cleaving angle of 1 degree was applied in the numerical model to mimic the fact that a perfect cleaving angle was hardly achieved experimentally. The simulation did not consider optical loss so that the maximum reflectance is almost 1. As one can see from Fig. 2(a), despite the difference in the overall reflectance, the shapes of the simulated and the measured transfer functions are quite consistent. The small parasitic resonant "dips" on both the measured and the simulated transfer functions are confirmed to be caused by non-ideal fiber cleaving.
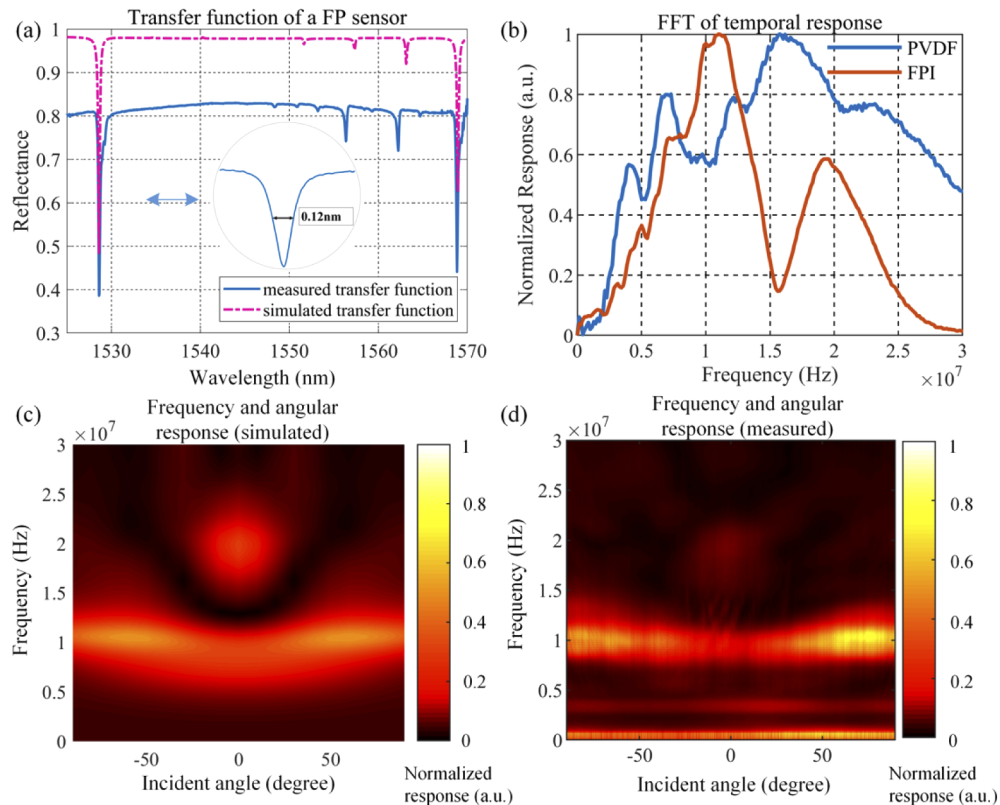
Fig. 2. (a) Measured and simulated transfer function of a representative FPI, inset shows a zoom-in view around the resonant wavelength. (b) Fast Fourier Transform (FFT) of the temporal response obtained by a FPI (orange) and a commercial PVDF hydrophone (blue). The incident acoustic pulses were generated by a 50 MHz water immersion transducer. (c) COMSOL simulation and (d) measured spectral response of the FP sensor under different acoustic incident angle.

Table 1. Optical parameters of a representative FPI (uncorrected values directly read from the OSA, which underestimate the sensor performance; FSR: free spectral range).

Parameter	Value
Thickness	19.9 μm
FSR	40.25nm
Finesse	329.9
Q-value	12811
Fringe visibility	0.3744
FWHM	0.12nm
Round trip loss	1.9%

Using a water immersion transducer (Olympus V358-SU) as the ultrasound source, we tested the acoustic response of a representative sensor. This transducer emitted ultrasound pulses with 50MHz central frequency. Figure 2(b) provides the fast Fourier transform from temporal signal received from FPI which demonstrates response frequency can reach 30MHz. It can be

found that the interferometer is resonant at about 10.5MHz and it has a weak response at around 15.5MHz. As for a comparison, the ultrasound source detected by a PVDF (Polyvinylidene fluoride) hydrophone (Precision Acoustics, NH0200) is plotted in the same figure. Note that these results were modulated by the spectral bandwidth of the 50 MHz source, and no deconvolution was performed. Directivity measurements were conducted using 1 MHz (Olympus V303-SU), 5 MHz (Olympus V310-SU), and 50 MHz single element transducers to synthesize a broadband acoustic source. Figure 2(c) shows the COMSOL simulation result of the sensor's response as a function of frequency and incident angle. This simulation utilized multi-physics coupling between two interfaces in COMSOL—"pressure acoustics, frequency domain" and "solid mechanics". During the simulation, planar acoustic waves with varying angle and frequency were incident on the FPI surface, and the sensor output as a function of these varying conditions was recorded to form a two-dimensional matrix. The simulation parameters used in COMSOL were the same as the actual sensor. We can learn from the simulation that this sensor is resonant at certain frequencies (depicted as the yellow zone) but has weak response at another frequencies (depicted as the dark zone). Figure 2(d) shows the measured directional response of the sensor, obtained by recording the signal strength at varying acoustical incidence angle. We can see a relatively flat response from −90° to 90° when the frequency is less than 15 MHz. The measured directional frequency response matches well with the COMSOL simulation. To measure the NEP, we used the hydrophone for pressure calibration. To do so, the hydrophone was held in close proximity to the FPI sensor, such that they probed a nearly uniform acoustic field. This allowed us to precisely determine the sensor's output at a given acoustic pressure. The NEP was acquired when the signal peak-to-peak voltage matches twice of the standard deviation of the noise. The NEP of the sensor was 220 Pa over a detection bandwidth of 30 MHz, or equivalently, 40 mPa/Hz$^{1/2}$.

3. Photoacoustic mesoscopic imaging

3.1. System setup

The whole photoacoustic mesoscopic imaging system consists of three sub-systems for PA excitation, FP sensor interrogation, and signal detection and processing, as shown in Fig. 3. In the PA excitation system, we use a 1064 nm nanosecond pulsed laser as the optical source to illuminate the imaging objects and excite photoacoustic signal. A Nd:YAG laser (LOTIS TII LS-2145-LT150) outputs various pulse energy with a fixed repetition rate of 10 Hz. The pulse duration is 40 ns, according to the output of a photodiode (Thorlabs, PDA10A2). The long pulse reduces the PA signal strength and worsens image resolution. During the experiment, the excitation light is collimated (Daheng Optics, GCO-140122) and shaped into a 20×20 mm^2 square light pattern, which illuminates the object uniformly. The imaging object is soaked in water in a customized container to facilitate acoustic coupling. The positions of the excitation light and the object are fixed during image acquisition. The XY motors in Fig. 3 consist of two motors moving orthogonally. One voice coil motor (VCM TECH, OWS120-25) translates the fiber FPI back and forth in the y direction. This motor is mounted on another step motor (Daheng Optics, GCD202050M) which moves along the x-axis unidirectionally. The combined movement of the two motors allows the FPI to be raster scanned over the imaged area. Before scanning, the FPI rests at one corner of the scanning grid. When scanning starts, the y-axis motor starts right away and moves along the + y direction. After it reaches y_{max}, the x-axis motor moves one step immediately and the y-axis motor starts to move in −y. Once it reaches y_{min}, the x-motor moves forward one more step. The above scanning process repeats until the entire grid is scanned. Both x- and y- translations are set to equal incremental step size of 100 µm. For the sensor interrogation system, we adopt a continuous wave laser (Pure Photonics, PPCL300) with narrow linewidth (10kHz) and low noise as the interrogation source. We fixed the output wavelength to 1550.12 nm. The laser light passes through a 3-port fiber circulator and a fiber coupler (Thorlabs, DC1300LEFA) to illuminate the FPI. Meanwhile, a power-adjustable 650 nm

diode laser (LaserWave, LWRL650nm-1W-F) is used as the heating laser. The 650 nm light passes through the same coupler (Thorlabs, DC1300LEFA) to set the working point of the FPI via photo-thermal heating. The fiber coupler (Thorlabs, DC1300LEFA) has a double clad fiber output port—the 650 nm light from one input port is coupled to its inner cladding while the 1550 nm light from another input port is coupled to its core. As a result, the 650 nm heating light and the 1550 nm interrogation light can be delivered simultaneously in the same fiber to illuminate the FPI. The average interrogation laser power incident on the fiber sensor is about 2 mW. Acoustic signal modulates the OPL of the sensing cavity of the FPI, and subsequently leads to a modulation of the reflected optical power. The reflected light goes backwards through the circulator and is finally detected by either the OSA or a customized InGaAs photo detector, where the alternating current (AC) and direct current (DC) components are separated. The AC channel has a 3 dB bandwidth of 30 MHz. A 16-bit 250MSamples/s data acquisition card (DAQ, Alazar Tech, ATS9350) captures the AC output of the photodetector and digitizes the analogue voltage signal. Ideally, the amplitude of the received signal is proportional to the instant PA pressure. Another DAQ (NI, USB-6002) with a sampling rate of 50 Ksamples/s is used to capture the DC output of the photodetector. Slow spectral shift of the sensor is indicated by the DC voltage, which controls the output power of the 650nm laser in real time through a feedback loop to stabilize the working point of the sensor. Signal acquisition and feedback control of the 650 nm laser are achieved by an automatic LabVIEW program.
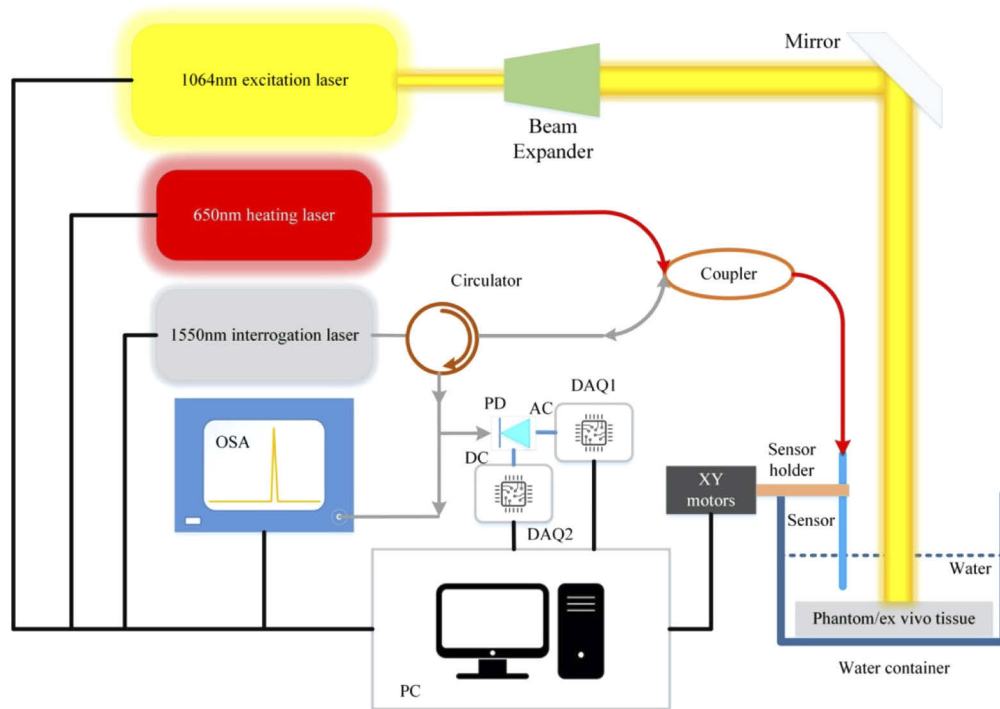

Fig. 3. Schematic of the imaging system. OSA: Optical spectrum analyzer. PD: Photo detector. AC: Alternate current. DC: Direct current. DAQ: Data acquisition card. PC: Personal computer.

In the imaging experiments, phantoms and *ex vivo* small animal organs were illuminated by the 1064 nm laser pulses with a maximum surface fluence of 20mJ/cm^2. The XY motors translated the imaging object within the laser spot to form a scanning area of 12.8×12.8 mm^2. A total number of 128×128 = 16384 points were scanned for each tomogram. The total scanning time for

an image was 1639s (16384 points divided by the excitation pulse repetition rate). After signal acquisition, a 3D delay-and-sum algorithm [42] was applied to reconstruct the photoacoustic images. Signals were not averaged during reconstruction.

3.2. Phantom imaging

We firstly demonstrated the imaging quality of the PA mesoscope using two different types of phantoms. The first phantom was made of human hairs and horse manes. We tied a knot using the two horse manes and embedded them into agarose to a depth around 4 mm. Then three human hairs were buried above manes and their depths were about 1~2 mm. A photo of the phantom is shown in Fig. 4(b), and the reconstructed tomogram is shown as maximum intensity projection (MIP) images in Fig. 4(a), provided in three orthogonal perspectives. The result matches perfectly with the photo and the designed target depths.
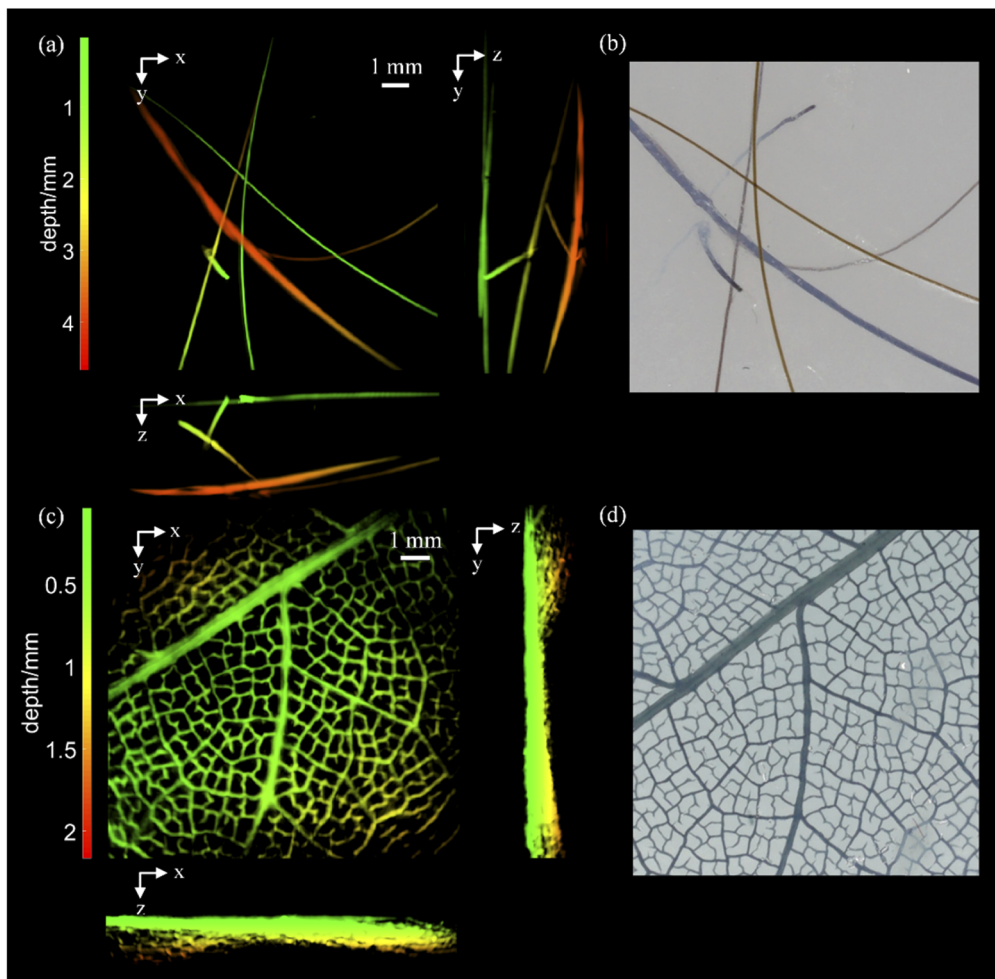

Fig. 4. (a) MIP images of the reconstructed phantom made of human hairs and horse manes. Projections in the x-y, y-z, and x-z planes are provided. (b) Photograph of the phantom in (a). (c) MIP images of the reconstructed leaf vein phantom. (d) Photograph of the leaf vein phantom.

The second phantom was fabricated by embedding a leaf vein in a piece of agar. The leaf was dyed with black ink so it can absorb light more efficiently. Figure 4(d) shows the photo of this leaf vein phantom and Fig. 4(c) provides the reconstructed tomogram, also shown as MIP images of three perspectives. The PA images matches well with the photo.

3.3.   *Ex vivo imaging*

An ex vivo mouse kidney was imaged and high-resolution PA images were reconstructed, as shown in Fig. 5. The mouse kidney was obtained from a NU/NU mouse (15 weeks). Main vessels were ligated before excision and we put the sample into paraformaldehyde immediately to preserve the blood inside the tissue. The PA images clearly show the vasculature of the kidney at depths, reaching up to 3mm.
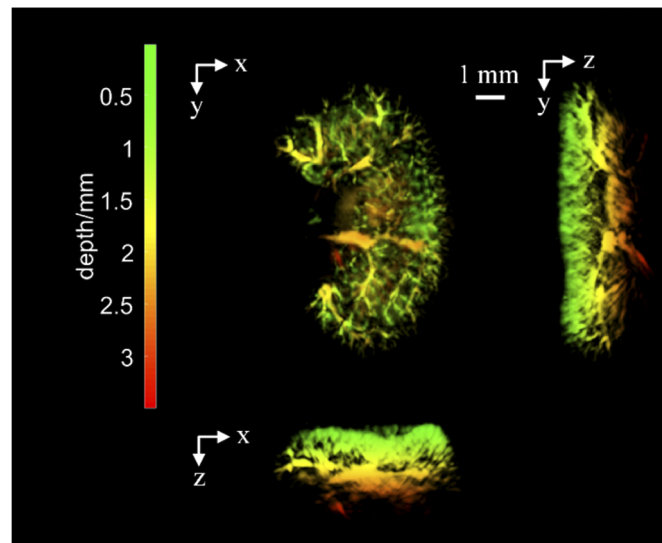

Fig. 5. MIP images of an *ex vivo* mouse kidney shown in x-y, y-z, and x-z planes.

4.   Discussion

We designed and realized a tunable fiber optic Fabry-Pérot interferometric acoustic sensor for photoacoustic mesoscopy. Spectral tuning of the sensor was realized using a 650 nm power-tunable diode laser. We used a relatively cheap, narrow-linewidth 1550 nm laser to interrogate the interferometer and set up a compact photoacoustic mesoscopic imaging system. Broadband, highly-sensitive acoustic detection was demonstrated by phantom and *ex vivo* tissue imaging.

The sensor is featured by its spectral tuning capability, which provides the opportunity for reducing the cost of PA mesoscopic imaging systems. For existing PA imaging systems that employ optical ultrasound sensors, their high costs are partially attributable to the interrogation laser. Since PA signals are weak, interferometric sensors often work under high quality factors. This renders the sensors susceptible to environmental instabilities, and makes real-time tracking of the optimal working point challenging. High precision tracking of the resonant peak/dip is always accomplished by high-end lasers featuring narrow-linewidth, low noise, fast and wide wavelength tuning capability. Such lasers are much more expensive than their fixed-wavelength counterpart—the price of the former usually exceeds $30,000 while the latter typically costs less than $5000. Besides, the heating laser used in this study costs only $1500. The reduction of interrogation cost makes sensor multiplexing economically feasible, which may benefit in vivo

imaging by boosting image acquisition speed. In contrast, non-ideal sensor uniformity and high interrogation cost make multiplexing extremely challenging using existing techniques.

The sensor fabrication process is compatible with batch-production. We have customized an automated dip-coating system which can fabricate tens of sensors simultaneously with good uniformity. To coat the cavity mirrors, hundreds of sensors can be processed at a time. In addition, the structure of the interferometer is relatively simple and robust, and the entire optical setup is alignment free.

Despite the above advantages, this sensor is still in its primitive stage. Firstly, the fiber sensor is fragile without suitable protection. Excessive care must be exerted handling the sensors before packaging is finished. Secondly, this sensor cannot work in water for a long time, otherwise the polymer spacer might swell to an extent to ruin the quality factor or to fail peak tracking. Even though recovery is possible by a well-designed drying remedy, the swelling problem can adversely affect user experience. Future improvements include an optimization of the spacer material, and adding a hydrophobic protective layer during sensor packaging. Thirdly, mechanical resonance of the cavity generates a ringing effect, exhibiting a spurious tail in the detected signal. Currently, this problem limits the spatial resolution and generates image artifacts. Further structural design is underway to deal with this problem. In the future, the image resolution of our system needs to be measured more accurately. Currently, the excitation pulse duration of 40 ns is too wide to yield a faithful resolution measurement. We have performed a line spread function measurement using a 9 µm diameter tungsten wire as the target. According to this test, the lateral resolution is 84 µm, while the axial resolution is 231 µm (the large axial resolution is tentatively due to a tail in the signal generated by acoustic resonance, which can be further suppressed by proper packaging). Lastly, the current imaging time of 1639s (∼27 minutes) for a scanning area of 12.8 mm × 12.8 mm is too long for clinical uses. This is mainly due to the low repetition rate (10 Hz) of the excitation laser we used in this experiment. In the future, with a faster excitation laser (such as 1000 Hz repetition rate), the imaging time can be decreased to several seconds for the same field of view.

5. Conclusion

We designed, fabricated, and demonstrated an optical fiber Fabry-Pérot interferometer for broadband acoustic sensing. The working point of the sensor can be photo-thermally tuned to support sustained image acquisitions at greatly reduced cost. The frequency response, sensitivity and angular response were experimentally characterized and demonstrated to be satisfactory. Using this sensor, we set up a low-cost photoacoustic mesoscopic imaging system and obtained images of two phantoms and an *ex vivo* mouse kidney. Potential impact of the sensor is further corroborated by the fact that it can be batch fabricated. Future endeavors include improved packaging, material selection, and sensor multiplexing.

Disclosures

The authors declare that there are no conflicts of interest related to this article.

References

1. L. V. Wang and J. Yao, "A practical guide to photoacoustic tomography in the life sciences," Nat. Methods **13**(8), 627–638 (2016).
2. M. Toi, Y. Asao, Y. Matsumoto, H. Sekiguchi, A. Yoshikawa, M. Takada, M. Kataoka, T. Endo, N. Kawaguchi-Sakita, M. Kawashima, E. Fakhrejahani, S. Kanao, I. Yamaga, Y. Nakayama, M. Tokiwa, M. Torii, T. Yagi, T. Sakurai, K. Togashi, and T. Shiina, "Visualization of tumor-related blood vessels in human breast by photoacoustic imaging system with a hemispherical detector array," Sci. Rep. **7**(1), 41970 (2017).
3. R. A. Kruger, C. M. Kuzmiak, R. B. Lam, D. R. Reinecke, S. P. Del Rio, and D. Steed, "Dedicated 3D photoacoustic breast imaging," Med. Phys. **40**(11), 113301 (2013).
4. L. Lin, P. Hu, J. Shi, C. M. Appleton, K. Maslov, L. Li, R. Zhang, and L. V. Wang, "Single-breath-hold photoacoustic computed tomography of the breast," Nat. Commun. **9**(1), 2352 (2018).
5. S. Y. Chuah, A. B. E. Attia, V. Long, C. J. H. Ho, P. Malempati, C. Y. Fu, S. J. Ford, J. S. S. Lee, W. P. Tan, D. Razansky, M. Olivo, and S. Thng, "Structural and functional 3D mapping of skin tumours with non-invasive multispectral optoacoustic tomography," Skin. Res. Technol. **23**(2), 221–226 (2017).
6. Y. Zhou, S. V. Tripathi, I. Rosman, J. Ma, P. Hai, G. P. Linette, M. L. Council, R. C. Fields, L. V. Wang, and L. A. Cornelius, "Noninvasive Determination of Melanoma Depth using a Handheld Photoacoustic Probe," J. Invest. Dermatol. **137**(6), 1370–1372 (2017).
7. J. Kim, Y. H. Kim, B. Park, H.-M. Seo, C. H. Bang, G. S. Park, Y. M. Park, J. W. Rhie, J. H. Lee, and C. Kim, "Multispectral ex vivo photoacoustic imaging of cutaneous melanoma for better selection of the excision margin," Br. J. Dermatol. **179**(3), 780–782 (2018).
8. J. Aguirre, M. Schwarz, N. Garzorz, M. Omar, A. Buehler, K. Eyerich, and V. Ntziachristos, "Precision assessment of label-free psoriasis biomarkers with ultra-broadband optoacoustic mesoscopy," Nat. Biomed. Eng. **1**(5), 0068 (2017).
9. M. Liu and W. Drexler, "Optical coherence tomography angiography and photoacoustic imaging in dermatology," Photochem. Photobiol. Sci. **18**(5), 945–962 (2019).
10. C. Lutzweiler, R. Meier, E. Rummeny, V. Ntziachristos, and D. Razansky, "Real-time optoacoustic tomography of indocyanine green perfusion and oxygenation parameters in human finger vasculature," Opt. Lett. **39**(14), 4061–4064 (2014).
11. M. Masthoff, A. Helfen, J. Claussen, A. Karlas, N. A. Markwardt, V. Ntziachristos, M. Eisenblätter, and M. Wildgruber, "Use of Multispectral Optoacoustic Tomography to Diagnose Vascular Malformations," JAMA Dermatol. **154**(12), 1457–1462 (2018).
12. A. A. Plumb, N. T. Huynh, J. Guggenheim, E. Zhang, and P. Beard, "Rapid volumetric photoacoustic tomographic imaging with a Fabry-Perot ultrasound sensor depicts peripheral arteries and microvascular vasomotor responses to thermal stimuli," Eur. Radiol. **28**(3), 1037–1045 (2018).
13. Y. Xu, L. V. Wang, G. Ambartsoumian, and P. Kuchment, "Reconstructions in limited-view thermoacoustic tomography," Med. Phys. **31**(4), 724–733 (2004).
14. G. Paltauf, R. Nuster, M. Haltmeier, and P. Burgholzer, "Experimental evaluation of reconstruction algorithms for limited view photoacoustic tomography with line detectors," Inverse Problems **23**(6), S81–S94 (2007).
15. V. Ntziachristos, "Going deeper than microscopy: the optical imaging frontier in biology," Nat. Methods **7**(8), 603–614 (2010).
16. M. Omar, J. Aguirre, and V. Ntziachristos, "Optoacoustic mesoscopy for biomedicine," Nat. Biomed. Eng. **3**(5), 354–370 (2019).
17. A. Maxwell, S. Huang, T. Ling, J. Kim, S. Ashkenazi, and L. J. Guo, "Polymer Microring Resonators for High-Frequency Ultrasound Detection and Imaging," IEEE J. Sel. Top. Quantum Electron. **14**(1), 191–197 (2008).
18. C. Zhang, S.-L. Chen, T. Ling, and L. J. Guo, "Review of imprinted polymer microrings as ultrasound detectors: Design, fabrication, and characterization," IEEE Sens. J. **15**(6), 3241–3248 (2015).
19. E. Zhang, J. Laufer, and P. Beard, "Backward-mode multiwavelength photoacoustic scanner using a planar Fabry-Perot polymer film ultrasound sensor for high-resolution three-dimensional imaging of biological tissues," Appl. Opt. **47**(4), 561–577 (2008).
20. S. Preisser, W. Rohringer, M. Liu, C. Kollmann, S. Zotter, B. Fischer, and W. Drexler, "All-optical highly sensitive akinetic sensor for ultrasound detection and photoacoustic imaging," Biomed. Opt. Express **7**(10), 4171–4186 (2016).
21. W. Rohringer, S. Preißer, M. Liu, S. Zotter, Z. Chen, B. Hermann, H. Sattmann, B. Fischer, and W. Drexler, "All-optical highly sensitive broadband ultrasound sensor without any deformable parts for photoacoustic imaging," in *Photons Plus Ultrasound: Imaging and Sensing 2016* (International Society for Optics and Photonics, 2016), p. 970815.
22. S. Ashkenazi, Y. Hou, T. Buma, and M. O'Donnell, "Optoacoustic imaging using thin polymer etalon," Appl. Phys. Lett. **86**(13), 134102 (2005).
23. A. Rosenthal, D. Razansky, and V. Ntziachristos, "High-sensitivity compact ultrasonic detector based on a pi-phase-shifted fiber Bragg grating," Opt. Lett. **36**(10), 1833–1835 (2011).
24. X. Zhu, Z. Huang, G. Wang, W. Li, D. Zou, and C. Li, "Ultrasonic detection based on polarization-dependent optical reflection," Opt. Lett. **42**(3), 439–441 (2017).
25. S. M. Maswadi, B. L. Ibey, C. C. Roth, D. A. Tsyboulski, H. T. Beier, R. D. Glickman, and A. A. Oraevsky, "All-optical optoacoustic microscopy based on probe beam deflection technique," Photoacoustics **4**(3), 91–101 (2016).

26. C. I. Zanelli and S. M. Howard, "Schlieren metrology for high frequency medical ultrasound," Ultrasonics **44**, e105–e107 (2006).
27. J. G. Laufer, E. Z. Zhang, B. E. Treeby, B. T. Cox, P. C. Beard, P. Johnson, and B. Pedley, "In vivo preclinical photoacoustic imaging of tumor vasculature development and therapy," J. Biomed. Opt. **17**(5), 056016 (2012).
28. J. Buchmann, J. Guggenheim, E. Zhang, C. Scharfenorth, B. Spannekrebs, C. Villringer, and J. Laufer, "Characterization and modeling of Fabry-Perot ultrasound sensors with hard dielectric mirrors for photoacoustic imaging," Appl. Opt. **56**(17), 5039–5046 (2017).
29. E. Z. Zhang, J. G. Laufer, R. B. Pedley, and P. C. Beard, "In vivohigh-resolution 3D photoacoustic imaging of superficial vascular anatomy," Phys. Med. Biol. **54**(4), 1035–1046 (2009).
30. R. Ellwood, O. Ogunlade, E. Zhang, P. Beard, and B. Cox, "Photoacoustic tomography using orthogonal Fabry–Pérot sensors," J. Biomed. Opt. **22**(4), 041009 (2016).
31. J. Laufer, F. Norris, J. Cleary, E. Zhang, B. Treeby, B. Cox, S. P. Johnson, P. Scambler, M. Lythgoe, and P. Beard, "In vivo photoacoustic imaging of mouse embryos," J. Biomed. Opt. **17**(6), 061220 (2012).
32. J. Guggenheim, T. Allen, A. Plumb, E. Zhang, M. Rodriguez-Justo, S. Punwani, and P. Beard, "Photoacoustic imaging of human lymph nodes with endogenous lipid and hemoglobin contrast," J. Biomed. Opt. **20**(5), 050504 (2015).
33. B. T. Cox and P. C. Beard, "The frequency-dependent directivity of a planar fabry-perot polymer film ultrasound sensor," IEEE Trans. Ultrason., Ferroelect., Freq. Contr. **54**(2), 394–404 (2007).
34. P. Morris, A. Hurrell, A. Shaw, E. Zhang, and P. Beard, "A Fabry–Pérot fiber-optic ultrasonic hydrophone for the simultaneous measurement of temperature and acoustic pressure," J. Acoust. Soc. Am. **125**(6), 3611–3622 (2009).
35. J. A. Guggenheim, J. Li, T. J. Allen, R. J. Colchester, S. Noimark, O. Ogunlade, I. P. Parkin, I. Papakonstantinou, A. E. Desjardins, E. Z. Zhang, and P. C. Beard, "Ultrasensitive plano-concave optical microresonators for ultrasound sensing," Nat. Photonics **11**(11), 714–719 (2017).
36. C. Villringer, T. Saeb Gilani, E. Z. Zhang, S. Pulwer, P. Steglich, S. Schrader, J. Laufer, A. A. Oraevsky, and L. V. Wang, "Development of tuneable Fabry-Pérot sensors for parallelised photoacoustic signal acquisition," presented at the Photons Plus Ultrasound: Imaging and Sensing 2019.
37. R. Ansari, E. Z. Zhang, A. E. Desjardins, and P. C. Beard, "All-optical forward-viewing photoacoustic probe for high-resolution 3D endoscopy," Light: Sci. Appl. **7**(1), 75 (2018).
38. G. Li, Z. Guo, and S.-L. Chen, "Miniature all-optical probe for large synthetic aperture photoacoustic-ultrasound imaging," Opt. Express **25**(21), 25023–25035 (2017).
39. E. Zhang and P. Beard, *Characteristics of Optimized Fibre-optic Ultrasound Receivers for Minimally Invasive Photoacoustic Detection* (SPIE, 2015).
40. R. Ansari, E. Zhang, S. Mathews, A. E. Desjardins, P. C. E. D. N. V. Beard, and R. Zemp, "Photoacoustic endoscopy probe using a coherent fibre-optic bundle," in *Opto-Acoustic Methods and Applications in Biophotonics II* (Optical Society of America, Munich, 2015), p. 953905.
41. E. Zhang and P. Beard, *A Miniature All-optical Photoacoustic Imaging Probe* (SPIE, 2011).
42. M. Xu and L. V. Wang, "Universal back-projection algorithm for photoacoustic computed tomography," Phys. Rev. E **71**(1), 016706 (2005).